ELSEVIER

Journal of Alloys and Compounds 452 (2008) 273–278

Journal of ALLOYS AND COMPOUNDS

www.elsevier.com/locate/jallcom

Corrosion and oxidation behavior of Pr-based bulk metallic glasses

Q.G. Meng, S.G. Zhang, J.G. Li *

School of Materials Science and Engineering, Shanghai Jiao Tong University, Shanghai 200030, China

Received 13 October 2006; received in revised form 29 October 2006; accepted 1 November 2006
Available online 30 November 2006

Abstract

The corrosion behavior of the quaternary Pr–Cu–Ni–Al bulk metallic glasses (BMGs) in 3.5 wt.% NaCl solution were investigated by potentiodynamic polarization and electrochemical impedance spectroscopic techniques. It is found that the there is a good correlation between the corrosion resistance and the glass-forming ability (GFA) in the BMGs, the larger the GFA, the stronger the corrosion resistance. In case of the representative $Pr_{55}Cu_{15}Ni_{15}Al_{16}$ BMG, the isothermal heat treatment was conducted and it was found that the corrosion resistance became smaller with holding time at 483 K. The thermogravimetry measurement on the Pr–Cu–Ni–Al BMGs showed that the oxidation resistance was deteriorated by increasing the Cu content and no correlations were found with the GFA. The composition of the scales formed during the oxidation was confirmed by X-ray diffraction. The corrosion and oxidation mechanisms were also discussed based on the experimental results.

Keywords: Amorphous materials; Corrosion; Glass-forming ability; Oxidation

1. Introduction

Since the first "bulk metallic glass" (BMG) Pd–Cu–Si was prepared by Chen in 1974 [1], many families of the bulk metallic glass-forming alloys including La–Al–Ni, Zr–Ti–Cu–Ni–Be, Zr–Ni–Al–Cu, Mg–Cu–Y and Pd–Cu–Ni–P have been discovered in the early1990s [2–5]. These new BMGs are expected to open up extensive applications due to their unique structures and properties. Among these, the rare-earth (RE) based BMGs offer great potential for application as functional materials [6,7].

For practical application of the RE-based BMGs, an understanding of the corrosion and oxidation behavior is needed. However, little work has been done on this topic. It is reported that many amorphous alloys has superior corrosion resistance due to their special structures without crystal boundary. Alvarez et al. [8] had explored the corrosion behavior of Ni–B–Sn melt-spun amorphous ribbons in NaCl solution with different pH values using Tafel experiments, and concluded that this amorphous alloy exhibits a better corrosion resistance than the crystalline counterpart; Qin et al. [9] used X-ray diffraction (XRD), Electrochemical impedance spectroscopy (EIS) and X-ray photoelectron spectroscopy (XPS) to monitor the corrosion behavior of $Zr_{55}Al_{10}Cu_{30}Ni_{5-x}Pd_x$ ($x = 0$, 5 at.%) BMG. The results showed that the difference in the corrosion behavior is originated from different glass-forming ability (GFA). On the other hand, only several investigations of oxidation behavior of conventional amorphous alloys (e.g. Zr-based and Fe-based amorphous alloys) are reported in the literature [10–13]. They considered that the oxidation behavior of the glass-forming alloys strongly depended on the alloy composition and microstructures. The oxides are likely to be formed first for the composition elements with large quantity and strong affinity for oxygen.

In this study, we focus on the corrosion and oxidation behavior of Pr–Cu–Ni–Al BMGs, and particularly on understanding the role of amorphous structure and alloy composition in the corrosion and oxidation mechanisms. Moreover, it is of interest to make a comparison between the corrosion and oxidation mechanisms as they are in nature all oxidation–reduction processes.

2. Experimental

The Pr-based master alloys with the nominal atomic percent compositions were prepared by arc melting Cu, Ni, Al with the purity of no less than 99.9 wt.% and Pr with the purity of no less than 99.7 wt.% in titanium-gettered argon atmosphere. Cylindrical specimens of 2 mm in diameter and 60 mm in length were prepared from the pre-alloys ingots by suction casting into a copper mold. The heat treatments were carried out in an evacuated quartz tube with a vacuum of 1×10^{-3} Pa. Thermal analysis was performed from the room temperature

* Corresponding author. Tel.: +86 21 62932569.
E-mail addresses: mggsjtu@sjtu.edu.cn, lijg@sjtu.edu.cn (J.G. Li).

0925-8388/$ – see front matter © 2006 Elsevier B.V. All rights reserved.
doi:10.1016/j.jallcom.2006.11.007

to the liquidus temperature (T_l) at a constant hearting rate of 10 K/min with a differential scanning calorimeter (DSC, Netzsch DSC 404C). The microstructure of samples was examined by XRD in a D/Max-rB diffractometer using Cu Kα radiation.

The cylindrical specimens for electrochemical tests were ground into an area of 0.2 cm × 0.5 cm at one end and a copper wire lead was attached with the silver paint to the other end. Except for the exposed surface for testing, the entire specimen was covered with an epoxy resin. The testing areas were mechanically polished with successive SiC papers of 240, 400 and 600 grain size, then were degreased with ethyl acetate and were washed with ethyl alcohol and distilled water before each experiment. Electrochemical measurements were carried out using a typical three-electrode system: a stationary specimen, a pair of counter electrodes (made of Pt sheet) and a saturated calomel reference electrode (SCE). A CHI 660 A electrochemical workstation was used for the polarization curves and the electrochemical impedance spectroscopy (EIS) measurements at room temperature after 20 min exposure to the test solution starting at the open-circuit potential. The test solution, 3.5 wt.% NaCl aqueous solution, was prepared with analytical grade NaCl reagent (≥99.5 wt.%) and deionized water. A scan rate of 0.8 mV/s was used for the potentiodynamic polarization test. The EIS method was used in the frequency range from 10^5 to 0.1 Hz and involved the imposition of a sine wave with 5 mV in amplitude. From potentiodynamic polarization curves and EIS results, the parameters related to corrosion were then obtained to analyze the electrochemical behavior of these BMGs. The BMGs for the oxidation experiments were sliced into Ø 4 mm × 0.5 mm and the experiments were carried out in dry air using a thermogravimetry analyzer (TG, Netzsch TG209).

3. Results

3.1. DSC measurement

Fig. 1 shows typical examples of DSC results for the as-cast Pr–Cu–Ni–Al BMGs in cylindrical shapes at a heating rate of 10 K/min. These alloys reveal sequential phase transition from amorphous state to the glass transition region, supercooled liquid region, fully crystallized state and melting region. The supercooled liquid region ΔT_x (=$T_x - T_g$) [14] became smaller and the crystallization process was split into two peaks in the sequence from $Pr_{54}Cu_{15}Ni_{15}Al_{16}$ to $Pr_{60}Cu_5Ni_{25}Al_{10}$ BMGs in Fig. 1, where the T_g and T_x represent the onset temperatures of glass transition and crystallization, respectively. All of the related thermodynamic parameters deduced from the DSC curves of Fig. 1 are summarized in Table 1. Many criterions have been proposed to evaluate the GFA [14–16], If ΔT_x and γ (=$T_x/(T_g + T_l)$) [16] are used as indicators of the GFA for the Pr–Cu–Ni–Al BMGs, it is obvious to see that ΔT_x and γ have the same tendency with compositions, and the GFA ranks from high to low as the following: $Pr_{54}Cu_{15}Ni_{15}Al_{16} > Pr_{60}Cu_{25}Ni_5Al_{10} > Pr_{60}Cu_{20}Ni_{10}Al_{10} > Pr_{60}Cu_{10}Ni_{20}Al_{10} > Pr_{60}Cu_5Ni_{25}Al_{10}$.

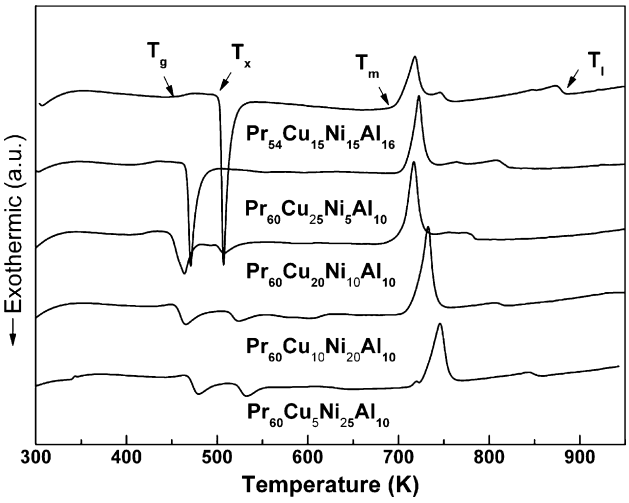

Fig. 1. DSC traces for Pr–Cu–Ni–Al bulk metallic glasses with the diameter of 2 mm at a heating rate of 10 K/min.

3.2. Electrochemical impedance spectroscopy

The impedance data of Pr–Cu–Ni–Al alloys in 3.5% NaCl solutions at room temperature were obtained after holding the samples at open-circuit potential for 20 min. Thus, it made all the samples get a stationary open-circuit potential before the test of EIS and potentiodynamic polarization experiments. Just like the $Pr_{60}Cu_5Ni_{25}Al_{10}$ Nyquist plot in Fig. 2(a), all the resulting Nyquist plots of Pr–Cu–Ni–Al alloys (Figs. 3 and 4) present only one capacitive loop, which are confirmed by the Bode plot of the impedance data in Fig. 2(b). The sole peak of the phase curve corresponds to the capacitive loop in the whole range of the experimental frequency. Then, we adopted several equivalent circuit models containing only one capacitive loop to fit the impedance data for such alloy system. The best fitting model can be represented by the equivalent circuit R(QR) (the inset of Fig. 2(a)) composed of one parallel RQ arrangement in series with the ohmic resistance whose mathematical expression of the impedance is given by:

$$Z = R_s + \frac{1}{j\omega Q_{dl} + (1/R_t)} = R_s + \frac{R_t}{1 + j\omega R_t Q_{dl}} \quad (1)$$

where R_s is the solution resistance, Q_{dl} the non-ideal double layer capacity and R_t is the electrochemical transfer resistance [17]. The constant phase elements, Q_{dl}, were used instead of pure capacities, C_{dl}, to represent the capacitive elements, taking account of the deviations of the system from the ideal state due

Table 1
Thermal properties deduced from the DSC measurements at a heating rate of 10 K/min, the values of the glass transition temperature T_g, the onset temperature of crystallization T_x, the onset melting temperature T_m, the offset melting temperature T_l, the supercooled liquid region ΔT_x and γ (=$T_x/(T_g + T_l)$) for the Pr–Cu–Ni–Al bulk metallic glasses

BMGs	T_g	T_x	T_m	T_l	ΔT_x	γ
$Pr_{54}Cu_{15}Ni_{15}Al_{16}$	465.4	515.5	696.7	882.3	50.1	0.383
$Pr_{60}Cu_5Ni_{25}Al_{10}$	417.6	465.8	707.1	819.7	48.2	0.376
$Pr_{60}Cu_{10}Ni_{20}Al_{10}$	413.9	449.0	689.9	784.8	35.1	0.374
$Pr_{60}Cu_{20}Ni_{10}Al_{10}$	435.0	454.4	707.4	819.3	19.4	0.362
$Pr_{60}Cu_{25}Ni_5Al_{10}$	450.5	467.1	714.3	854.5	16.6	0.358

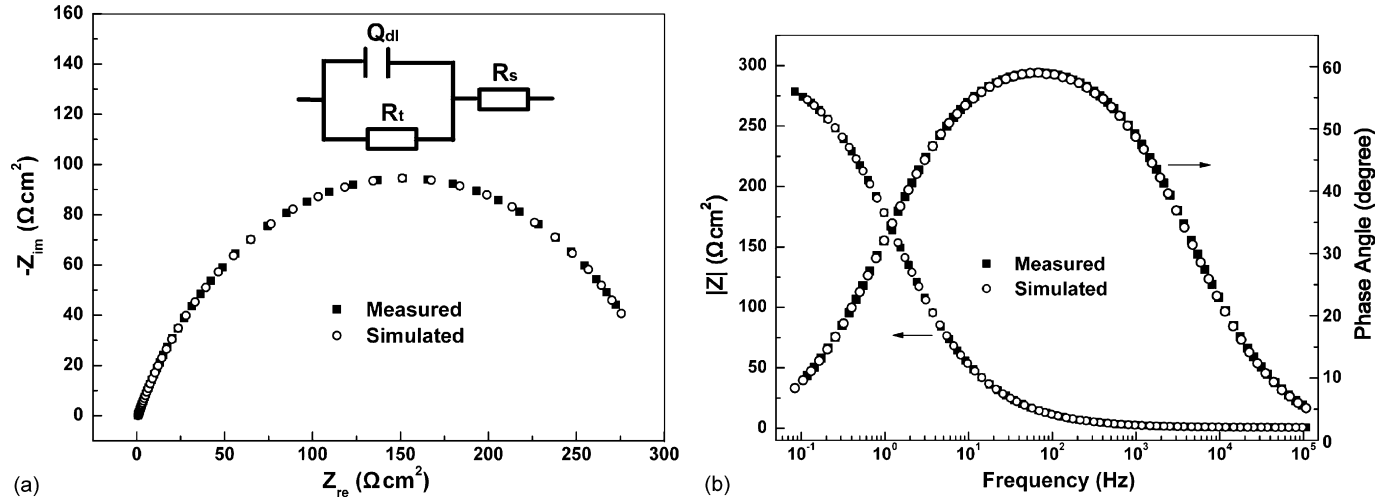

Fig. 2. Experimental Nyquist plot (a), Bode plot (b) and the fitted plot of $Pr_{60}Cu_5Ni_{25}Al_{10}$ BMG in 3.5% NaCl solution at open-circuit after 20 min immersion. The inset of (a) is the fitting equivalent circuit.

to surface heterogeneities and other possible reasons [18]. The impedance of a constant phase element, CPE, is defined as:

$$Q_{\mathrm{dl}} = (\mathrm{j}\omega)^{-n/Y_0} \tag{2}$$

where Y_0 is the admittance constant and n is a fit parameter related to the extent of the dispersion which is induced by the surface inhomogeneity. For Eq. (1), the impedance Z is a transfer function of multiple variables (i.e. R_s R_t, Q_{dl} and ω). Nevertheless, once the parameters for the circuit elements are determined through modeling, the impedance Z is simply a function of frequency ω, which produces an EIS spectrum.

Data fitting and element analysis were carried out by using non-linear least squares (NLLS) simulating software. A good fit for the EIS data (hollow dots) of $Pr_{60}Cu_5Ni_{25}Al_{10}$ BMG was shown in Fig. 2. The corrosion current density at E_{corr} can be calculated from the impedance data by the expression (3) proposed by Diard et al. [19]:

$$i_{\mathrm{corr}} = \frac{RT}{FnR_t} \tag{3}$$

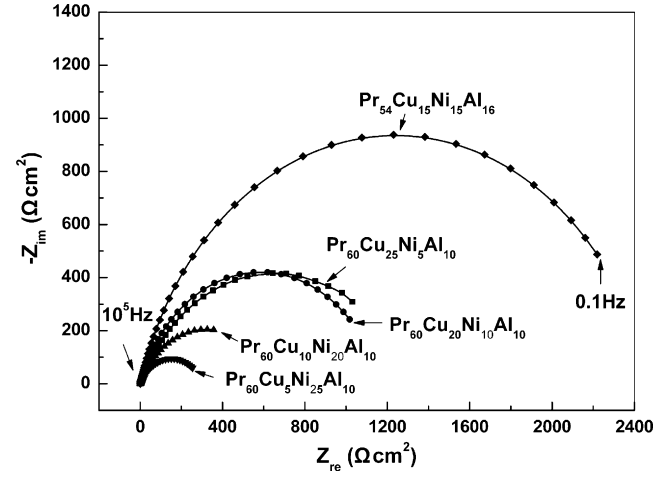

Fig. 3. Experimental Nyquist plots of Pr–Cu–Ni–Al bulk metallic glasses in 3.5% NaCl solution after holding the samples at open-circuit potential for 20 min.

where R is the gas constant, T the temperature, F the constant of Faraday and n is the fit parameter of Q_{dl}. Fig. 3 shows the experimental Nyquist plots of Pr–Cu–Ni–Al BMGs in 3.5% NaCl solution after holding the samples at open-circuit potential for 20 min. The fitting parameters and the corrosion current density i_{corr} calculated by Eq. (3) are listed in Table 2.

It can be seen from Fig. 3 that the capacitive loops become larger at low frequency, and follow the sequence of increase from $Pr_{60}Cu_5Ni_{25}Al_{10}$ to $Pr_{54}Cu_{15}Ni_{15}Al_{16}$ BMG. This indicates the corrosion resistance increases in this order which satisfies well with the R_t and i_{corr} variation trends listed in Table 2. Larger R_t and smaller i_{corr} mean higher corrosion resistance. Furthermore, there is a good correlation between the corrosion resistance and the glass-forming ability in the alloy system. The larger the GFA indictor γ or ΔT_x, the higher the corrosion resistance for the BMG in this particular environment.

In order to study the effect of the microstructure on the corrosion resistance for the Pr–Cu–Ni–Al glass-forming alloys, the

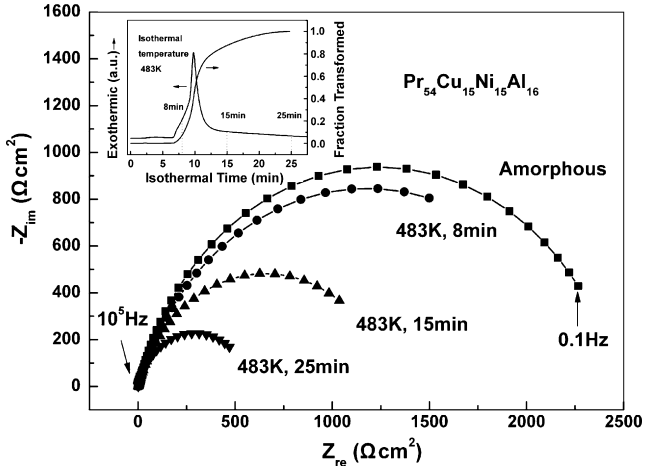

Fig. 4. Experimental Nyquist plot of $Pr_{54}Cu_{15}Ni_{15}Al_{16}$ BMG in 3.5% NaCl solution after holding the samples at open-circuit potential for 20 min. The inset is the isothermal heat treatment of the $Pr_{54}Cu_{15}Ni_{15}Al_{16}$ BMG at 483 K for different duration time.

Table 2
Impedance parameter values of electrochemical transfer resistance (R_t), the non-ideal double layer capacity (Q_{dl}), and solution resistance (R_s), corrosion current density (i_{corr}) calculated from EIS data for the Pr–Cu–Ni–Al alloys in 3.5% NaCl solution after holding the samples at open-circuit potential for 20 min

Alloys	Treatment status	R_s (Ω cm^2)	R_t ($\times10^3$ Ω cm^2)	Q		i_{corr} (10^{-5} A cm^{-2})
				Y_0 ($\times10^{-4}$ S cm^2)	n ($0<n<1$)	
$Pr_{54}Ni_{15}Cu_{15}Al_{16}$	Amorphous	0.600	2.479	0.913	0.825	1.264
	483 K, 8 min	0.145	2.355	6.839	0.794	1.382
	483 K, 15 min	1.102	1.309	7.534	0.809	2.441
	483 K, 25 min	0.958	0.582	4.667	0.844	5.263
$Pr_{60}Cu_{25}Ni_5Al_{10}$	Amorphous	0.836	1.302	3.645	0.725	2.739
$Pr_{60}Cu_{20}Ni_{10}Al_{10}$	Amorphous	0.739	1.167	1.871	0.796	2.783
$Pr_{60}Cu_{10}Ni_{20}Al_{10}$	Amorphous	0.717	0.640	12.459	0.725	5.571
$Pr_{60}Cu_5Ni_{25}Al_{10}$	Amorphous	0.732	0.303	9.179	0.710	12.016

$Pr_{54}Cu_{15}Ni_{15}Al_{16}$ BMG was chosen as a representative. The BMG was treated at 483 K for different duration time in order to obtain different crystallization structures. The three selected points of isothermal time, 8, 15 and 25 min, were located in the front semi-peak, the rear semi-peak and the end of the peak, respectively. The corresponding experimental Nyquist plots of $Pr_{54}Cu_{15}Ni_{15}Al_{16}$ alloy after the treatment in 3.5% NaCl solution are shown in Fig. 4. It can be seen that the capacitive loops become smaller with increasing the isothermal crystallization time, indicating that the corrosion resistance become weaker with the increase of the crystalline volume fraction. The fitting parameters according to Eq. (1) and the related corrosion current density i_{corr} calculated by Eq. (3) are also listed in Table 2. The R_t and i_{corr} have a good correlation and agree well with the radii of the capacitive loops shown in Fig. 4.

3.3. Potentiodynamic polarization results

The typical potentiodynamic polarization curves of Pr–Cu–Ni–Al alloys, obtained in 3.5% NaCl solutions open to air at 298 K, are shown in Figs. 5 and 6, where E is the potential and i is the polarization current density. The experimental conditions of Figs. 5 and 6 are just the same as those of Figs. 3 and 4, respectively. It can be seen that the potentiodynamic polarization curves of all the alloys have a similar profile, and shows no obvious current plateau which is associated with a passive film formation at anodic polarization sides. However, the alloys show quick dissolution at the anodic sides with increasing E. As the Tafel regions are only shown in the curves of cathodic polarization sides, we can use these curves to gain the kinetic parameters of corrosion such as cathodic Tafel slope (β_c) and corrosion current density (i_{corr}).

The polarization kinetic parameters (β_c, i_{corr}) and the corrosion potential (E_{corr}) were determined using the Tafel slope method [20] from Figs. 5 and 6 and were summarized in Table 3. As the current density of each sample is approximately linear with the potential within $\pm$25 mV in the potentiodynamic polarization curve, the slope of this plot from a tangent at E_{corr} defines the polarization resistance R_p which is also shown in Table 3.

Generally, smaller corrosion current density (i_{corr}) and larger polarization resistance (R_p) mean higher corrosion resistance. Seen from Figs. 5 and 6 and Table 3, the i_{corr} of the BMG samples is in the following sequence: $Pr_{54}Cu_{15}Ni_{15}Al_{16}$ < $Pr_{60}Cu_{25}Ni_5Al_{10}$ < $Pr_{60}Cu_{20}Ni_{10}Al_{10}$ < $Pr_{60}Cu_{10}Ni_{20}Al_{10}$ < $Pr_{60}Cu_5Ni_{25}Al_{10}$. This signifies that the corrosion resistance is becoming stronger from the $Pr_{60}Cu_5Ni_{25}Al_{10}$ to $Pr_{54}Cu_{15}Ni_{15}Al_{16}$ BMGs and agrees well with the same ranking of the

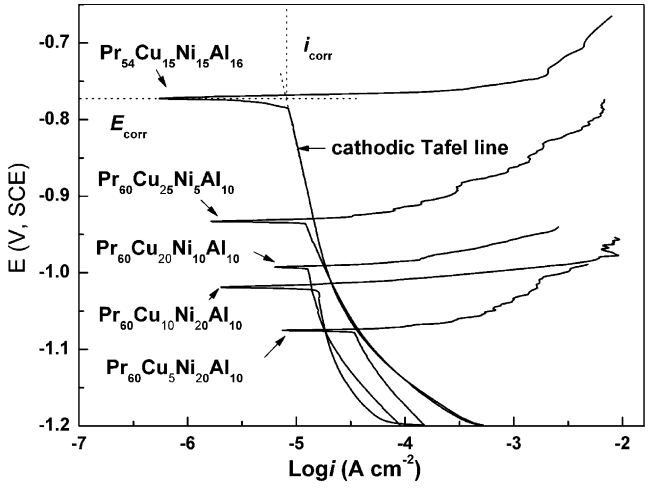

Fig. 5. The potentiodynamic polarization curves in E vs. log i of Pr–Cu–Ni–Al BMGs in 3.5% NaCl solution.

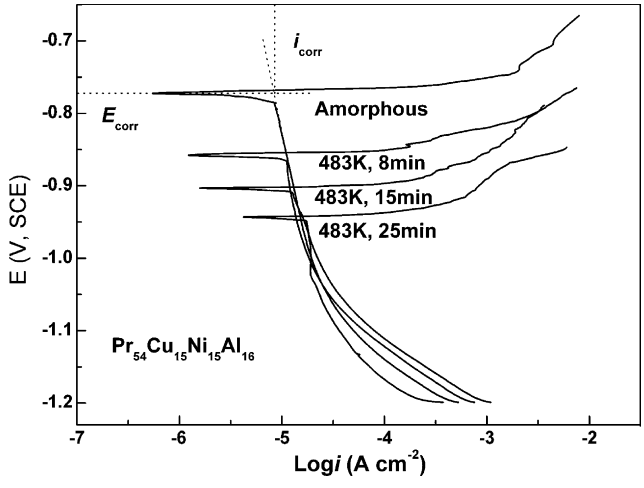

Fig. 6. The potentiodynamic polarization curves in E vs. log i of the $Pr_{54}Cu_{15}Ni_{15}Al_{16}$ BMG in 3.5% NaCl solution. The BMG was heat treated at 483 K for different duration time.

Table 3
Polarization resistance (R_p), cathodic Tafel slope (β_c), and corrosion current density (i_{corr}) calculated from polarization data in 3.5% NaCl solution of the Pr–Cu–Ni–Al BMGs after holding the samples at open-circuit potential for 20 min

Alloys	Treatments	R_p ($\times 10^3\ \Omega\ cm^2$)	β_c (V)	E_{corr} (V)	i_{corr} ($\times 10^{-5}$ A cm^{-2})
$Pr_{54}Cu_{15}Ni_{15}Al_{16}$	Amorphous	2.850	−1.58	−0.773	0.851
	483 K, 8 min	2.104	−1.212	−0.857	1.047
	483 K, 15 min	1.106	−2.680	−0.904	1.200
	483 K, 25 min	0.515	−0.56	−0.944	1.778
$Pr_{60}Cu_{25}Ni_5Al_{10}$	Amorphous	1.673	−3.185	−0.933	1.164
$Pr_{60}Cu_{20}Ni_{10}Al_{10}$	Amorphous	0.990	−1.482	−0.993	1.274
$Pr_{60}Cu_{10}Ni_{20}Al_{10}$	Amorphous	0.917	−1.185	−1.018	1.580
$Pr_{60}Cu_5Ni_{25}Al_{10}$	Amorphous	0.272	−4.183	−1.076	3.311

R_p and E_{corr}. The R_p increase from 12.074 to 1079.607 Ω cm^2 and the E_{corr} from −1.076 to −0.773 V. In case of the $Pr_{54}Cu_{15}Ni_{15}Al_{16}$ BMG after isothermal heat treatment at 483 K, the i_{corr} increases while the R_p and the E_{corr} decrease with the holding time. Thus, the corrosion resistance deduced from the potentiodynamic polarization experiments is consistent with what obtained from the EIS data.

3.4. Thermogravimetry measurement

Fig. 7 shows the variation of weight gain per unit area with temperature for the Pr–Cu–Ni–Al BMGs in static air at a heating rate of 5 K/min. The oxidation of the samples exhibits a linear behavior below the onset temperature of the BMG melting, then the gain weight starts to increase sharply in the melting region, and at last is followed by a steady-state after the offset temperature of the BMG melting. Thus, it can be concluded that the oxygen-diffusion is the controlling process for the BMG oxidation processes. The $Pr_{60}Cu_{25}Ni_5Al_{10}$ is mostly prone to be oxidized among all of the four BMGs. On the contrary, the oxidation resistance of the $Pr_{60}Cu_5Ni_{25}Al_{10}$ BMG is the best. Thus, there is a correlation between the oxidation resistance and the Cu content in the BMGs. The less the Cu content, the stronger the oxidation resistance in the four BMGs. Similar results are also found by Köster et al. [12] in the Zr-based metallic glasses that the oxidation resistance was deteriorated by the addition of Cu. However, there is no correlation between the oxidation resistance and the GFA, indicating that the decisive factors for the corrosion and oxidation resistance are different although the processes are all oxidation–reduction reactions.

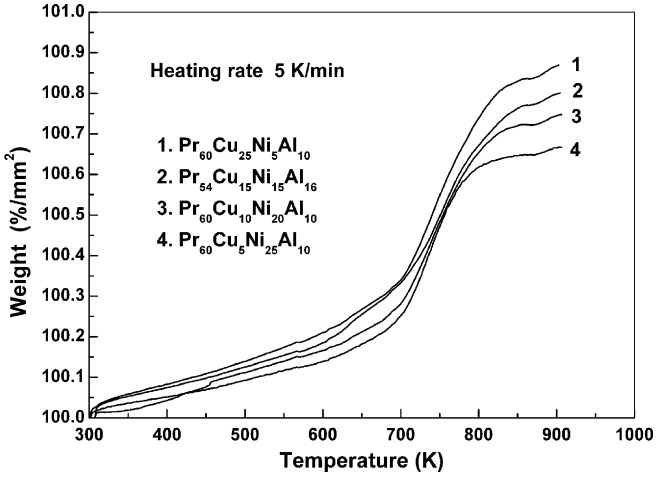

Fig. 7. Variation of weight gain with temperature for the Pr–Cu–Ni–Al BMGs in static air at a heating rate of 5 K/min.

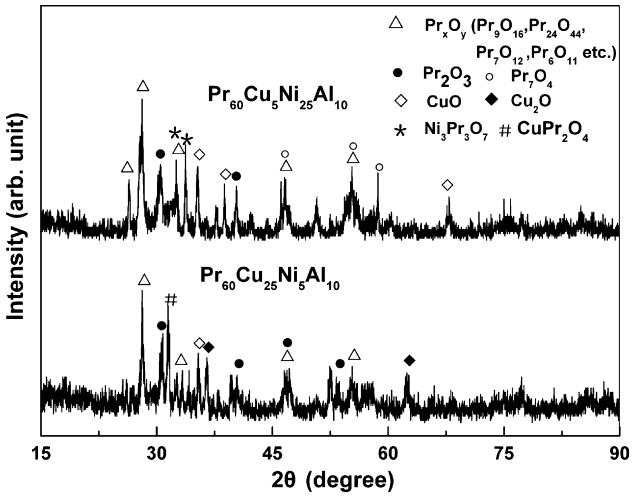

Fig. 8. XRD patterns of the surface oxides of $Pr_{60}Cu_5Ni_{25}Al_{10}$ and $Pr_{60}Cu_{25}Ni_5Al_{10}$ BMGs which were heated up to 730 K at a heating rate 5 K/min in static air.

In order to analyze the oxidation mechanism of the Pr-based BMGs, the X-ray diffraction pattern of the oxide scales formed on the representative $Pr_{60}Cu_{25}Ni_5Al_{10}$ and $Pr_{60}Cu_5Ni_{25}Al_{10}$ BMGs at 730 K in air at a heating rate of 5 K/min are indexed and shown in Fig. 8. The oxide scale of $Pr_{60}Cu_5Ni_{25}Al_{10}$ alloy mainly consists of the oxides of Pr (e.g. Pr_7O_{12}, Pr_2O_3, etc.) with minor amounts of CuO and $Ni_3Pr_3O_7$ oxides. The oxide scale of $Pr_{60}Cu_{25}Ni_5Al_{10}$ alloy mainly contains the oxides of Pr and Cu, e.g. Pr_7O_{12}, Pr_2O_3, CuO and Cu_2O, etc., and no oxide of Ni is found for both of the alloys. Thus, the Cu reacts with oxygen even with low composition content, however the Ni does not seem combine with oxygen even with high composition content.

4. Discussion

As the results shown above, the corrosion resistance for the Pr–Cu–Ni–Al BMGs deduced from the potentiodynamic

polarization experiments agrees well with what obtained from the EIS data when the BMGs are put into 3.5% NaCl solutions for electrochemical tests, the following reactions are considered as the anodic reactions [21]: $Al \rightarrow Al^{3+} + 3e^-$; $Pr \rightarrow Pr^{3+} + 3e^-$; $TM \rightarrow TM^{x+} + xe^-$, where TM represents Cu and Ni; The cathodic reactions of corrosion are primarily related to the oxygen reduction and hydrogen evolution. Then the cathodic reactions generate an alkaline environment that leads to localized precipitation of hydrated oxides such as $Pr(OH)_3$, Pr_2O_3, PrO_2, $TM(OH)_x$, TM_xO_y, etc., and thus the formation of the surface protective film [22]. Generally, it is considered that metal ions with lower valences such as Pr^{3+}, Cu^+ are in transitional status, the oxides and hydroxide with high valences (e.g. PrO_2) are mainly formed into the compositions of protection film [23]. Cl^- ions of the solution are absorbed on the metal surface in competition with the dissolved O^{2-} or OH^- and favor the hydration of metal ions to enter into solution. Hence, Cl^- will prevent the formation of the surface protection film [9]. According to Figs. 5 and 6, there is no obvious current plateau of passivation in the experimental range, and thus the samples dissolve rapidly at the anodic sides. Furthermore, it can be concluded that the corrosion resistance of the alloys in this study mainly depends on their structures besides the compositions. The fact that the amorphous alloys with larger GFA and short-time heat treatment showed superior corrosion resistance can be attributed to their less degree of the crystalline defects and the chemical homogeneity.

Oxidation resistance of the Pr–Cu–Ni–Al BMGs was found to be deteriorated by increasing the content of Cu and have no correlations with the GFA. Sharma et al. [10] studied the oxidation behavior of Zr-based BMGs ($Zr_{65}Cu_{17.5}Ni_{10}Al_{7.5}$ and $Zr_{46.75}Ti_{8.25}Cu_{7.5}Ni_{10}Be_{27.5}$) and explained the formation of the oxides from the perspective of the heat of formation. The heat of the formation for Al_2O_3, NiO and CuO are −1117.6, −4997.7 and −314.8 kJ/mol O_2, respectively [24]. The oxide formation is closely related to the affinity between the components and oxygen. According to this, the first formation of the Pr_xO_y and Al_2O_3 oxides would retard the migration of the oxygen through the oxide film. However, only from the points of formation heats and the diffusion behavior of the alloys elements, it is difficult to explain the effect of Cu on the oxidation behavior of our BMGs. In fact, the catalytic activity of Cu, which accelerates the reaction of Pr with oxygen and thus takes part in the oxidation reaction, is considered as the dominant factor in the oxidation behavior of the Pr–Cu–Ni–Al BMGs. Therefore, the different mechanisms of the oxidation–reduction reactions resulted in no correlations between the corrosion and oxidation resistance.

5. Conclusions

From the experimental results and discussion presented above, several conclusions can be drawn as follows:

1. There is a good correlation between the corrosion resistance and the GFA, and the larger the GFA, the higher the corrosion resistance. The corrosion resistance of the Pr–Cu–Ni–Al BMGs are mainly depends on their structures.
2. Concerning the corrosion current and the polarization or electrochemical charge transfer resistance data, the values obtained by polarization experiments agrees well with those deduced from EIS data.
3. The thermogravimetry measurement on the Pr–Cu–Ni–Al BMGs showed that the oxidation resistance was deteriorated by increasing the Cu content, which resulted from the catalytic activity of Cu that accelerates the reaction of Pr with oxygen. The different mechanisms of the oxidation–reduction reactions resulted in no correlations between the corrosion and oxidation resistance.

Acknowledgements

The financial support from the National Science Foundation of China Grant Nos. 50274051 and 50125101 is gratefully acknowledged.

References

[1] H.S. Chen, Acta Metall. 22 (1974) 1505.
[2] A. Inoue, T. Zhang, T. Masumoto, Mater. Trans. JIM 30 (1989) 965.
[3] A. Inoue, T. Zhang, N. Nishiyama, Mater. Trans. JIM 34 (1993) 1234.
[4] A. Peker, W.L. Johnson, Appl. Phys. Lett. 63 (1993) 2342.
[5] A. Inoue, K. Ohtera, K. Kita, T. Masumoto, Jpn. J. Appl. Phys. 27 (1988) L2248.
[6] A. Takeuchi, A. Inoue, Mater. Sci. Eng. A 375–377 (2004) 1140–1144.
[7] A. Inoue, Mater. Sci. Eng. A 226–228 (1997) 357–363.
[8] M.G. Alvarez, S.M. Vazquez, F. Audebert, H. Sirkin, Scripta Mater. 39 (1998) 661–668.
[9] F.X. Qin, H.F. Zhang, P. Chen, F.F. Chen, D.C. Qiao, Z.Q. Hu, Mater. Lett. 58 (2004) 1246–1250.
[10] S.K. Sharma, T. Strunskus, H. Ladebush, F. Faupel, Mater. Sci. Eng. A 304–306 (2001) 747.
[11] H.H. Hsieh, W. Kai, R.T. Huang, M.X. Pan, T.G. Nieh, Intermetallics 12 (2004) 1089.
[12] Triwikantoro, D. Toma, M. Meuris, U. Köster, J. Non-Cryst. Solids 250–252 (1999) 719.
[13] H.H. Hsieh, W. Kai, R.T. Huang, C.Y. Lin, T.S. Chin, Intermetallics 14 (2006) 917.
[14] M.L.F. Nascimento, L.A. Souza, E.B. Ferreira, E.D. Zanotto, J. Non-Cryst. Solids 351 (2005) 3297.
[15] X.F. Bian, B.A. Sun, L.N. Hu, Y.B. Jia, Phys. Lett. A 335 (2005) 61–67.
[16] Z.P. Lu, C.T. Liu, Acta Mater. 50 (2002) 3503.
[17] C.N. Cao, Corrosion Electrochemistry, Chemical Industry Press, Beiing, 1985.
[18] A. Altube, A.R. Pierna, Electrochim. Acta 49 (2004) 303–311.
[19] J.P. Diard, B. Le Gorrec, C. Montella, J. Elechtrochim. Chem. 326 (1992) 13–36.
[20] C.M.A. Brett, A.M. Oliviera Brett, Electrochemistry: Principles, Methods and Applications, Oxford University Press, Oxford, 1998.
[21] S. Sunada, K. Majima, Y. Akasofu, Y. kaneko, J. Alloys Compd. 408–412 (2006) 1373–1376.
[22] M.F. Montemor, A.M. simÕes, M.G.S. Ferreira, Progress Org. Coat. 43 (2001) 274.
[23] N. Mora, E. Cano, J.L. Polo, J.M. Puente, J.M. Bastidas, Corros. Sci. 46 (2004) 563–578.
[24] D.R. Lide (Ed.), CRC Handbook of Chemistry and Physics, 76th ed., CRC Press, Boca Raton, 1995–96, pp. 34–47.